ICCFD13-2026-282

Modelling and simulation of atmospheric entry on ice giants with hybrid multi-temperature/state-to-state based model

D. Di Marzio[a], G. Diaferia[b], P. Nagy[a], D. Ninni[b], F. Bariselli[d], F. Bonelli[b], A. Laricchiuta[c], G. Colonna[c], G. Pascazio[b], M. Fossati[a]
Corresponding author: domenico.di-marzio@strath.ac.uk
[a] Aerospace Centre, Dept. Mechanical and Aerospace Engineering, University of Strathclyde, UK
[b] Dept. of Mechanics, Mathematics and Management, Polytechnic University of Bari, ITA
[c] Institute for Plasma Science and Technology, CNR, ITA
[d] von Karman Institute for Fluid Dynamics, BE

Abstract: Today, more than ever, physical and numerical modeling of atmospheric entry flows is one of the primary research focuses of the CFD community. During the entry phase, a body crosses the atmosphere and encounters a rarefied gas that becomes progressively denser with decreasing altitude. In the present work, the continuum regime is considered such that the gas is dense enough to be treated as a continuum medium and the Navier–Stokes equations apply. Strong bow shocks form in front of the body, and the temperature across them reaches thousands of kelvin, triggering non-equilibrium effects such as dissociation and ionization of the gas molecules. To account for these effects, the most common approach is to use the two-temperature model by Park. Although many research and commercial CFD codes use this model or some of its variants, it has been shown that it cannot reproduce the full spectrum of non-equilibrium gas dynamics. Hence, a reduced state- to-state model is considered for the simulation of atmospheric entry on Uranus and Neptune, and an operator-splitting technique is used to separate the physical processes for improved computational efficiency. The solutions are obtained with the CPU-based code SU2-NEMO and compared to those obtained with the GPU-based code DAMISO.

Keywords: State-To-State, Operator Splitting, Space Exploration, Ice Giants.

1. Introduction

The complex physical and chemical mechanisms make the simulation of atmospheric entry flows a difficult task. The temperature behind strong bow shocks reaches thousands of kelvin; this triggers chemical reactions such as dissociation and ionization changing the composition and the thermodynamic state of the gas medium. To model these effects, the two-temperature (2T) model by Park [1] has become a widely-adopted option in the majority of commercial and research CFD codes due to its simplicity and effectiveness. Although the two-temperature model performs well for a wide range of flows, it is not able to reproduce some important aspects of non-equilibrium flows [2, 3] and for this reason more advanced models have been considered by the scientific community. One model that is expected to provide better insight into the nonequilibrium processes typical of high-Mach and high-enthalpy flows is the so-called state-to-state model (StS) [4, 5, 6]. By accounting explicitly for the excitation of electronic states of the species in the gas, it is expected that the non-equilibrium energy exchange during particle collisions is represented more accurately allowing for a better understanding of these mechanisms in the case of potentially complex flows and allowing for a model that better predicts aerothermal loads on vehicles intended to operate at hypersonic regimes and/or undergoing atmospheric (re-)entry. In the present work, an hybrid multi-temperature/state-to-state (mT/StS) model is considered [7, 8], assigning a vibrational temperature to the ground electronic state of diatomic molecules and treating some electronic excited states of atoms and molecules in a StS framework, whereas translational and rotational energies are

considered in equilibrium with each other. This model has been constructed for the H_2/He mixture [9] derived from a StS model applied to Saturn entry. Hence, each electronic state is treated as a pseudo-species, whose spatio-temporal evolution is described by transport equations just like the case of true species. The atmospheric entry on ice giants was considered as test case. The simulations were performed with SU2 NEMO [10], a package that implements the Mutation++ [11] thermochemistry library in the SU2 CFD suite. In order to run simulations efficiently and efficiently, two different numerical schemes were used; these will be explained in more detail in the results section. Specifically, these were a fully implicit scheme and a semi-implicit scheme. For the semi-implicit scheme, the stiffness of the chemical source terms in the species mass balances are addressed using a sequential operator splitting method (also known as fractional step method). By means of operator splitting, an implicit scheme is used to solve the chemistry sub-step without the very demanding time step restriction and an explicit scheme is used for the transport sub-step with the classical advection-diffusion CFL requirement. The results of the entry trajectories in Neptune and Uranus are presented. Code verification is performed by comparing the results with those obtained with the code DAMISO [12] developed at the Polytechnic University of Bari.

2. Methodology

The CPU-based SU2-NEMO and the GPU-based DAMISO are both based on a finite volume approach. In both codes the continuum flow in thermochemical nonequilibrium can be written as a system of partial differential equations:

$$\mathbf{R}(\mathbf{U}, \nabla\mathbf{U}) = \frac{\partial \mathbf{U}}{\partial t} + \nabla \cdot \mathbf{F}^c(\mathbf{U}) - \nabla \cdot \mathbf{F}^v(\mathbf{U}, \nabla\mathbf{U}) - \mathbf{Q}(\mathbf{U}) = 0, \tag{1}$$

where the terms are the conservative variables $\mathbf{U}$, the convective flux $\mathbf{F}^c$, the viscous flux $\mathbf{F}^v$ and the source terms $\mathbf{Q}$ and n_s is the total number of species (or pseudo-species as in the StS approach):

$$\mathbf{U} = \begin{pmatrix} \rho_1 \\ \vdots \\ \rho_{n_s} \\ \rho\mathbf{u} \\ \rho e \\ \rho e^{v,H_2} \end{pmatrix}, \ \mathbf{F}^c = \begin{pmatrix} \rho_1\mathbf{u} \\ \vdots \\ \rho_{n_s}\mathbf{u} \\ \rho\mathbf{u}\mathbf{u} + p\mathbf{I} \\ \rho h\mathbf{u} \\ \rho e^{v,H_2}\mathbf{u} \end{pmatrix}, \ \mathbf{F}^v = \begin{pmatrix} -\mathbf{J}_1 \\ \vdots \\ -\mathbf{J}_{n_s} \\ \boldsymbol{\sigma} \\ \mathbf{u}\boldsymbol{\sigma} - \mathbf{q}^{tr} - \mathbf{q}^{v,H_2} - \sum_s \mathbf{J}_s h_s \\ -\mathbf{q}^{tr} - \mathbf{q}^{v,H_2} - \sum_s \mathbf{J}_s e^{v,H_2} \end{pmatrix}, \ \mathbf{Q} = \begin{pmatrix} \dot{\omega}_1 \\ \vdots \\ \dot{\omega}_{n_s} \\ 0 \\ 0 \\ \dot{\omega}^{v,H_2} \end{pmatrix}. \tag{2}$$

In the hybrid mT/StS model the equations are formally the same but n_s does not refer to the chemical species that make the mixture, instead it refers to all the pseudo-species, hence the chemical species with their electronic modes. In both models the mixture viscosity, thermal conductivity and diffusivity are computed starting from single species values. The state-to-state methodology was introduced in Mutation++, even though this branch is still not open-source as the work is under development and verifications are ongoing. A sequential operator splitting approach [13] is used to separate the problem into two different sub-problems. The spatial discretization is performed and a system of ODEs is obtained:

$$\begin{cases} \dfrac{d\mathbf{U}}{dt} = \mathbf{F}_A(\mathbf{U}) + \mathbf{F}_D(\mathbf{U}) + \mathbf{F}_R(\mathbf{U}), & x \in \Omega, \quad t > 0, \\ \mathbf{U} = \mathbf{U_D}, & x \in S_D, \quad t > 0, \\ \partial_n \mathbf{U} = \mathbf{U_N}, & x \in S_N, \quad t > 0, \end{cases} \tag{3}$$

where $\mathbf{F}_A$, $\mathbf{F}_D$ and $\mathbf{F}_R$ represent the advection, diffusion and reaction operators respectively. S_D and S_N are, respectively, the portions of the boundary of the physical domain Ω where Dirichlet and Neumann boundary conditions are applied. Then, the source terms are separated from the advection and diffusion

terms, obtaining the two sub-problems:

$$\begin{cases} \dfrac{d\mathbf{U}^*}{dt} = \mathbf{F}_R(\mathbf{U}^*), \text{ on } (t^n, t^{n+1}), \ \mathbf{U}^*(t^n) = \mathbf{U}^n & \text{(4a)} \\ \dfrac{d\mathbf{U}^{**}}{dt} = \mathbf{F}_A(\mathbf{U}^{**}) + \mathbf{F}_D(\mathbf{U}^{**}), \text{ on } (t^n, t^{n+1}), \ \mathbf{U}^{**}(t^n) = \mathbf{U}^*(t^{n+1}) & \text{(4b)} \end{cases}$$

with $\mathbf{U}^{n+1} = \mathbf{U}^{**}(t^{n+1})$. The equations (4a) and (4b) are solved sequentially for every time-step where the solution of equations (4a) is used as initial condition for equations (4b). The particular choice of splitting source terms from transport terms is done so that equations (4a) represent an initial value problem and no boundary conditions are required. A different splitting of the original system (3) would introduce an additional error if boundary conditions are not modified accordingly [13]. Of course, the splitting error is still present if the advection-diffusion and reaction operators do not commute, making the sequential splitting first-order in time [14]. More evolved splitting strategies can be employed, like Strang splitting [15], to reach second order convergence if the sub-steps schemes are at least second-order accurate. However, since the main problem with non-equilibrium external flows is the stability of the scheme, for the moment, the sequential splitting approach was believed to be sufficient. The splitting strategy enabled the use of different time integration schemes to solve the sub-steps. Specifically, an implicit scheme used to solve the sub-step (4a) and an explicit scheme for the sub-step (4b). The time-step is the same for both sub-steps such that the requirement of the advection-diffusion CFL condition is fulfilled.

3. Pseudo state-to-state model

A detailed state-to-state kinetic model was developed by G. Colonna, L. D. Pietanza, and A. Laricchiuta at CNR-ISTP Bari. The mechanism includes the species $H, H^+, H^-, H_2^+, H_3^+, He, He^+, He^{++}$, and e^-, with H and H_2 and the first three and four excited levels of H and H_2, respectively. To describe electronically excited molecular states with improved accuracy, the model uses a revised set of electron-impact cross sections. Singlet states are subdivided into vibrational levels, while state-specific Einstein coefficients and quenching processes are included; the latter contribute to molecular dissociation. The reduced model adopts a two-temperature formulation to decrease the cost associated with fully vibrationally resolved states. Starting from the state-to-state database, the chemical reaction rates and the characteristic frequencies for internal-temperature relaxation are expressed as functions of the relevant temperatures. Heavy species are assumed to be in equilibrium at the roto-translational temperature T_{tr}. Molecular hydrogen is assigned a vibrational temperature $T_v^{H_2}$. Finally, H and H_2 remain electronically resolved. Doubly ionized helium is retained only for the evaluation of thermodynamic properties. Although He^{++} becomes important at thermochemical equilibrium above $50000K$, the ionization of He^+ is not included in the chemical mechanism because it is inefficient as a reaction pathway.

Name	**Thermodynamic model**	**Electronic states**
H		1 ground + 3 excited states
H^+		Only ground state
H^-		Only ground state
H_2	RRHO	1 ground + 4 excited states
H_2^+	RRHO	Only ground state
H_3^+	RRHO	Only ground state
He		Only ground state
He^+		Only ground state
e^-		

Table 1: Thermodynamic model and electronic states for the considered species.

3.1 Thermodynamic properties

The thermodynamic properties of pure gases are derived from statistical mechanics through the corresponding partition functions. For example, if the different energy modes are assumed to be separable, the energy of a species, or pseudo-species, it can be written as the sum of the contributions associated with each independent mode. The Rigid-Rotor-Harmonic-Oscillator thermodynamic model is suitable for thermal non-equilibrium calculations. In multi-temperature models, the number of energy equations is equal to the number of independent global energy modes. The energy exchanged between these modes is not determined explicitly by the governing equations and must therefore be represented through modeled source terms. The state model used in the present work implements a two-temperature formulation with the following thermal non-equilibrium assumptions: $T_t = T_r, T_v = T_e = T_{fe}$. It can be applied to electronically resolved levels, including the hybrid formulation employed in the present work. Internal energy can be obtained from partition functions as follows:

$$e_i = e_i^t(T_t) + \sum_{\eta \in \mathcal{M}_i^{\text{int}}} e_i^\eta(T_{\eta,i}) + e_i^0, \tag{5}$$

$$e_i^t = \frac{3}{2} R_i T_{t,i}, \tag{6}$$

$$e_i^\eta = R_i T_{\eta,i}^2 \frac{\partial \log Q_i^\eta}{\partial T_{\eta,i}}. \tag{7}$$

This definition of internal energy is applicable both to multi-temperature models and to state-specific models, provided that the appropriate temperature and partition function are used for each mode. The remaining thermodynamic properties can be obtained in an analogous way [16].

3.2 Transport properties

In Mutation++, transport fluxes are evaluated using a multiscale Chapman-Enskog perturbative solution of the Boltzmann equation [17]. This approach yields asymptotic expressions for the transport coefficients, including viscosity, thermal conductivity, and diffusion coefficients. The coefficients are computed from linear transport systems, using a Laguerre-Sonine polynomial expansion to approximate the Enskog solution with increasing accuracy. The collision-integral database is organized into different interaction classes, such as neutral-neutral, ion-neutral, electron-neutral, charge-charge, and electron-electron collisions. These transport data were taken from [18] and were already available in the Mutation++ database. Only ground-state species are assumed to contribute to transport. For charge-charge interactions, collisions between charged particles are described using a screened Coulomb potential, shielded over the Debye length, where $z_i z_j$ is the product of the charges of the colliding species. The Debye length λ_D defines the characteristic distance over which charged particles are shielded from the surrounding plasma. In Mutation++, only electrons are considered in the shielding, and therefore the Debye length is written as in eq. 9 [19] derived an integration procedure for the Coulomb potential and expressed the main collision integral as a function of a reduced temperature T^* expressed in eq. 10.

$$\phi_{ij}(r) = \frac{z_i z_j}{r} \frac{q_e^2}{4\pi\epsilon_0} \exp\left(-\frac{r}{\lambda_D}\right), \tag{8}$$

$$\lambda_D^2 = \frac{\epsilon_0 k_B T_{\text{fe}}}{2 q_e^2 n_e} \tag{9}$$

$$T^* = 4\pi\epsilon_0 \frac{\lambda_D k_B T_{\text{fe}}}{q_e^2}. \tag{10}$$

The dynamic viscosity μ and the thermal conductivity λ_h are obtained from the first Laguerre-Sonine polynomial approximation of the Chapman-Enskog expansion. The resulting expression requires the

solution of the following linear systems:

$$\begin{cases} \mu = \sum_{i\in\mathcal{H}} \alpha_i^{\mu} x_i, \\ \sum_{j\in\mathcal{H}} G_{ij}^{\mu} \alpha_j^{\mu} = x_i, \qquad \forall i \in \mathcal{H}, \end{cases} \tag{11}$$

$$\begin{cases} \lambda_h = \sum_{i\in\mathcal{H}} \alpha_i^{\lambda_h} x_i, \\ \sum_{j\in\mathcal{H}} G_{ij}^{\lambda_h} \alpha_j^{\lambda_h} = x_i, \qquad \forall i \in \mathcal{H}. \end{cases} \tag{12}$$

Here, G_{ij}^{μ} and $G_{ij}^{\lambda_h}$ are obtained from the collision integrals.

3.3 Kinetic mechanism

For each reaction, the molar rate of progress can be written as follows:

$$\mathcal{R}_r = K_{f_r} \prod_{i\in\mathcal{S}^*} \left(\frac{\rho_i}{\mathcal{M}_i}\right)^{\nu'_{ir}} - K_{b_r} \prod_{i\in\mathcal{S}^*} \left(\frac{\rho_i}{\mathcal{M}_i}\right)^{\nu''_{ir}}. \tag{13}$$

Here, $\mathcal{M}_i$ denotes the molar mass of the corresponding species or pseudo-species, while $\mathcal{K}_f$ and $\mathcal{K}_b$ are the forward and backward reaction-rate coefficients. The mass production rate of the i-th pseudo-species, $\dot{\omega}_i$, is then computed from the law of mass action as follows:

$$\dot{\omega}_i = \mathcal{M}_i \sum_{r\in\mathcal{R}} \left(\nu''_{ir} - \nu'_{ir}\right) \mathcal{R}_r. \tag{14}$$

Four additional rate laws were implemented in the Mutation++ library. A generic independent temperature is denoted by T_η, where the subscript may be $\eta = tr, fe, v$, depending on the physical process being modeled. The new rates laws are shown in Table 8 in Appendix A. The kinetic mechanism can be divided in three classes of reactions: excitation/de-excitation reactions of molecular and atomic hydrogen depicted in Table 5 in Appendix A., the radiative kinetics made of radiative recombination, bound-bound transition (spontaneous emission) and photo-dissociation reactions in Table 6 in Appendix A., and finally chemical kinetics in Table 7 Appendix A. The chemical kinetics reactions give rise to two ionization paths. The first starts with H_2 dissociation by impact with heavy particles but ionization proceeds with associative ionization rather than heavy-impact ionization. Then, the kinetics proceeds dissociating molecular hydrogen and ionization of atomic hydrogen by by electron impact. The second ionization path begins with the exchange reactions between ground levels of molecular hydrogen that produce H_3^+ and H^-. These to species unfold different branches of the mechanism:

Table 2: Ionization path initiated by the presence of H_3^+ *(left)* and H^- *(right)*

$H_3^+ + e^- \rightleftharpoons H_2(0) + H(0)$	$H^- + H^+ \rightleftharpoons H(i) + H(0)$
$H_3^+ + e^- \rightleftharpoons H(0) + H(0) + H(0)$	$H^- + H_2^+ \rightleftharpoons H_2(0) + H(0)$
$H_3^+ + H(0) \rightleftharpoons H_2^+ + H_2(0)$	$H^- + e^- \rightleftharpoons H(0) + e^- + e^-$
$H_2^+ + H(0) \rightleftharpoons H^+ + H_2(0)$	$H^- + H_2(0) \rightleftharpoons H(0) + e^- + H_2(0)$
$H_2^+ + e^- \rightleftharpoons H(0) + H^+ + e^-$	$H^- + He \rightleftharpoons H(0) + e^- + He$
	$H^- + H(0) \rightleftharpoons H_2(0) + e^-$
	$H^- + H^+ \rightleftharpoons H_2^+ + e^-$
	$H^- + H_2^+ \rightleftharpoons H_3^+ + e^-$

P [Pa]	T [K]	T_v [K]	Δt [s]	Y_{H_2} [-]	Y_{He} [-]
46664	36000	1000	1×10^{-10}	0.81	0.19

Table 3: Initial conditions for the thermal reactors

3.4 Energy transfer terms

Vibration-heavy translation and free electron-heavy translation energy exchanges are taken from the CNR-ISTP Bari model. Chemistry-vibration coupling is described using the classical Candler non-preferential model [20]. The model also includes chemistry-electronic and chemistry-free-electron coupling. In addition, it accounts for the loss of energy from the electron thermal bath due to electron-impact reactions, including ionization, excitation, and dissociation. It accounts for energy losses associated with bound-bound radiative transitions in a transparent gas. In general, these energy-transfer mechanisms can be grouped into relaxation processes and chemical energy-exchange processes. All the energy transfer terms, including the new relaxation processes and the CNR-ISTP models, are described in Appendix B.

4. Use cases

This Section presents the application of the proposed methodology to 0D and 2D use cases representing respectively the nonequilibrium processes happening inside a thermal reactor and the non-equilibrium processes established in proximity of the blunt nose of a vehicle at atmospheric entry conditions.

4.1 0D Thermal Reactors

This section presents a comparison of the results in 0D thermal reactors between the CPU code SU2-NEMO and the GPU code DAMISO. Before the assessment of the differences, the focus must be on some significant differences in the thermochemical models used by the two codes. The first difference is in the chemistry-vibration transfer term model; DAMISO uses the fit law by CNR-ISTP whereas SU2-NEMO relies on the Mutation++ library, in which the fit law is not implemented and models the term as explained in 7. The second difference is in the kinetic mechanism; in Mutation++ H_2 dissociate by impact with the heavy species H_2 and H regardless of it's electronic level, but in DAMISO the ground level does not, i.e., eqs. 1.1 and 2.1 in Table 7 are not present in the kinetic mechanism used by DAMISO. Moreover, heavy-impact dissociation of H_2 due to collisions with He only exists for the ground level of H_2 (eq.3 in Table 7) while the kinetic mechanism of DAMISO only considers this dissociation reaction for the excited levels of H_2 . The third difference is the absence of an electron-impact dissociation reaction that produces a hydrogen cation H^+. Essentially, the following reaction is considered by the kinetic mechanism of DAMISO but not the one presented in this work:

$$\mathrm{H_2(0) + e^- \rightleftharpoons H(0) + H^+ + e^- + e^-}, \tag{15}$$

which affects the production of atomic hydrogen and hydrogen cation. Three thermal reactor simulations were performed, with the same initial conditions listed in Table 3, with three different mixtures (and associated mechanisms). The first is a simplified mixture of neutral species and its kinetic mechanism activates the dissociation reactions of H_2 only. The code to code comparison is shown in Fig. 1. The difference in temperature profiles highlights the effect of the different models for the chemistry-vibration source term in the vibrational energy equation. Thermal relaxation is faster in SU2-NEMO with the vibrational temperature that reaches a much higher peak value. In DAMISO, when molecular hydrogen is completely dissociated and its mass concentration reaches the equilibrium value, the vibrational temperature abruptly increases and equilibrates with the translational temperature. The higher value of T_v in the relaxation region is also reflected in the dissociation rate of H_2. From the mass fractions plot in fig. 1 it is clear how the dissociation rate in SU2-NEMO increases with respect to that of DAMISO

as the vibrational temperatures difference increases. Consequently, the mass fractions reach chemical equilibrium faster. The values of temperature and mass fractions at equilibrium is the same for the two codes, with only a slight difference in H_2 mass fraction of the order $O(10^{-5})$.

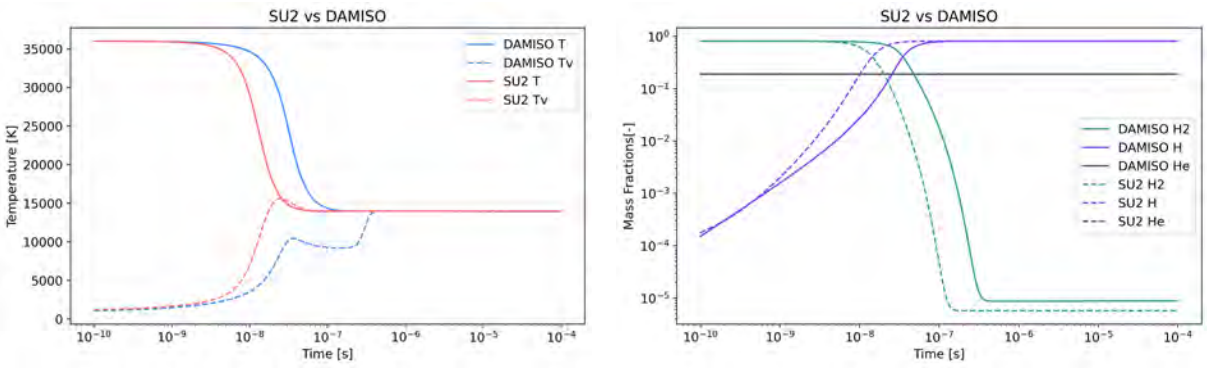

Figure 1: Neutral mixture thermal bath profiles in time. Temperatures *(left)* and mass fractions *(right)*.

The second thermal reactor simulation was performed with the complete mixture. However, the radiative processes of the kinetic mechanism were de-activated. The temperatures profiles shown in fig. 2 are qualitatively different. Compared to DAMISO results, in the first portion of the relaxation process, the vibrational temperature is in very good agreement while the translational temperature relaxes faster. The peak of vibrational temperature is again much higher for SU2-NEMO but thermal equilibrium is reached quicker. Just like the previous case, in DAMISO thermal equilibrium is reached when molecular hydrogen reaches its equilibrium value. After 1 μs, the temperature of SU2-NEMO starts decreasing and reaches the equilibrium value, equal to that of DAMISO. This is followed by a settling of H_2 mass fraction to its equilibrium value. Contrary to the neutral mixture case, in the first 10ns of simulation, the mass fraction of atomic hydrogen is lower than that of DAMISO, this is believed to be due to the lack of reaction in eq. 15. The same missing reaction in the mechanism is believed to cause the lower production of ionized species shown in Fig. 3. A lower concentration of H^+ implies a lower production of H_2^+ and H_3^+. From the evolution of ionized species is clear that the effect of H_2 recombination is to increase the mas fractions of ionized species since it reactivates dissociative attachment, electron impact and charge exchange processes.

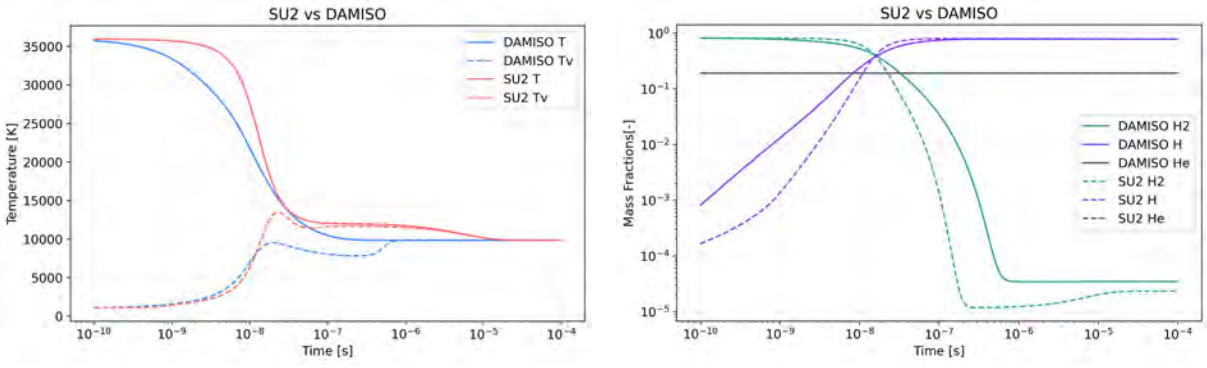

Figure 2: Full mixture thermal bath without radiative processes profiles in time. Temperatures *(left)* and neutral species mass fractions *(right)*.

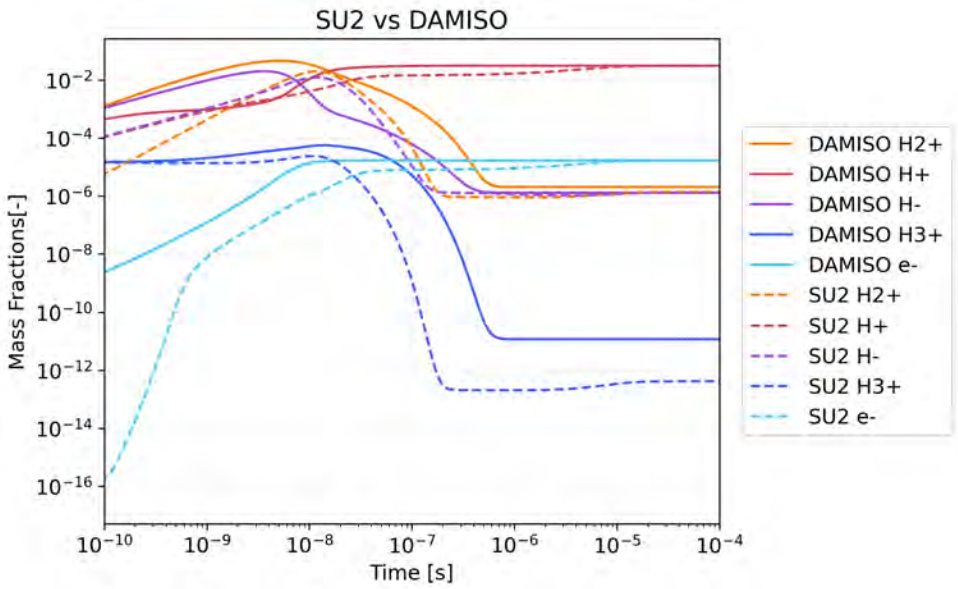

Figure 3: Full mixture thermal bath without radiative processes profiles in time. Ionized species mass fractions.

The results of the third thermal bath are very similar but highlight the effect of radiative emission on the temperatures and mixture composition. The effect of photon emission is to reduce the total energy of the plasma, this can be seen in fig. 4 as the temperature profiles of both DAMISO and SU2-NEMO keep decreasing after reaching thermal equilibrium. Both neutral and ionized species evolutions, shown in fig. 4 and fig. 5 respectively, are very similar to those of the full mixture without radiation. The main effect of temperature decrease on species mass fractions is a continued recombination of H_2. Without radiative processes, hydrogen recombination was followed by an increase in ions mass fractions; instead, fig. 5 shows that after a slight increase they start decreasing. This is due to the radiative recombination of H^+ which, in turns, produces a reduction of concentration of the other ions, prevailing on the chemical kinetics associated to the increase in H_2.

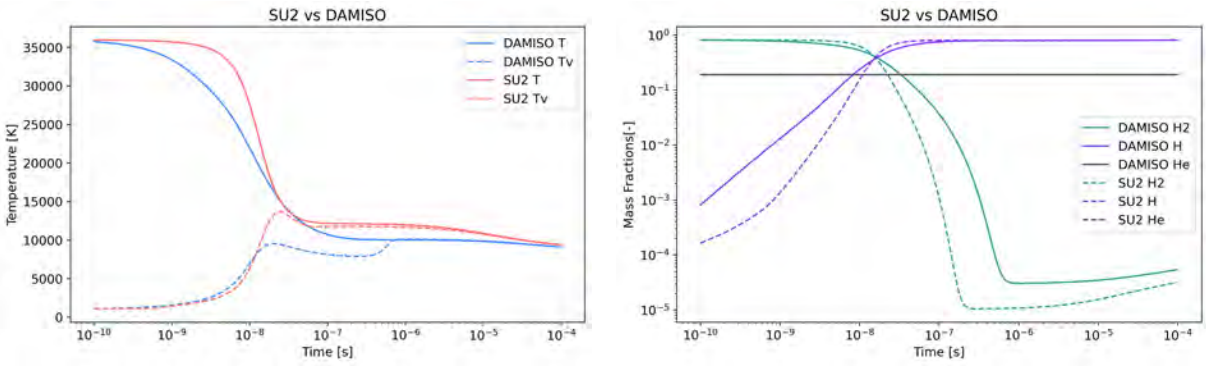

Figure 4: Full mixture thermal bath with full reaction mechanism profiles in time. Temperatures *(left)* and neutral species mass fractions *(right)*.

P [Pa]	T [K]	T_v [K]	Ma [-]	Y_{H_2} [-]	Y_{He} [-]	T_w [K]
22	300	300	18.15	0.74	0.26	3258

Table 4: Initial conditions for the 2D flow around a cylinder

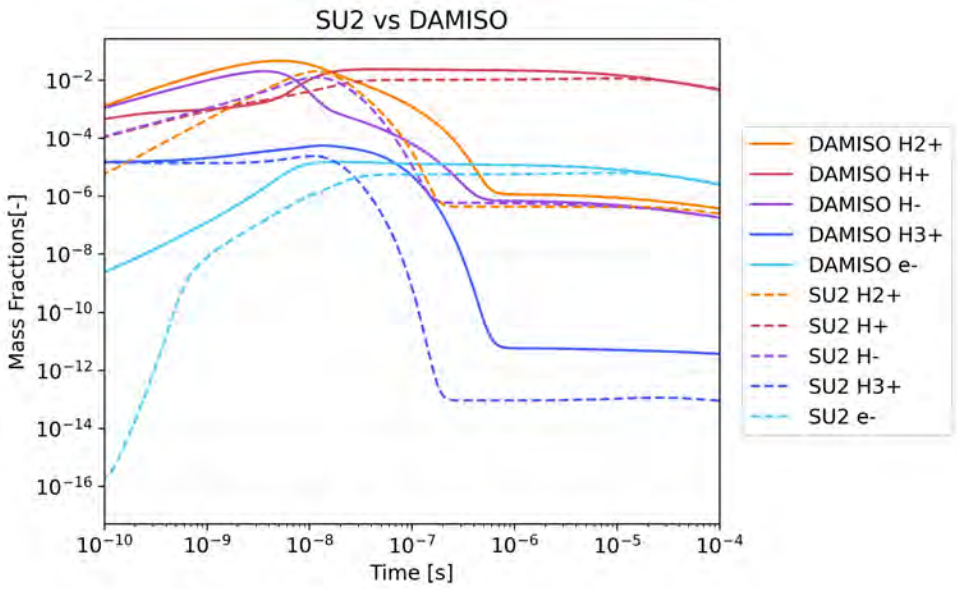

Figure 5: Full mixture thermal bath with full mechanism profiles in time. Ionized species mass fractions.

4.2 2D Flow Past a Cylinder

Two 2D planar simulations were performed over a cylinder with isothermal surface at temperature T_w = 3258 K; the freestream conditions were chosen to represent re-entry on an ice giant planet and are listed in Table 4. The simulations were performed with a classic 2T model and the pseudo-STS model. All 2D simulations used neutral mixtures since appropriate boundary conditions for ionized mixtures are currently under development. The solution for the multi-temperature case has been obtained using the operator-splitting approach to reduce the computational effort of a fully implicit approach. However, in the case of the STS mixture, the large number of reactions made the use of a fully implicit approach essential to speed up the calculation. The mesh used for the simulations is a structured grid of 150 thousand elements. The grid was refined in the boundary layer with a minimum Δy of 10^{-6} m at the wall and at the shock location. Figure 6 shows the profiles of the temperatures and the mass fractions on the stagnation line. Across the shock, the translational temperature peak is remarkably lower in the STS results, while the vibrational temperature peak only differs slightly. The STS results show a shorter relaxation time, but both simulations reach the same equilibrium temperature. Figure 7 shows the contours of translational and vibrational temperatures and the difference between the two, highlighting the thermal non-equilibrium region just downstream of the shock wave. Despite the marked difference in the maximum translational temperature, the mass fractions for atomic and molecular hydrogen are very similar in the two cases. The STS model produces a faster dissociation of H_2. Figure 6 shows the profiles for the excited states of both atomic and molecular hydrogen. The population of the excited states are very small if compared to the ground states. It is noteworthy that the second and third excited states of H do not appear.

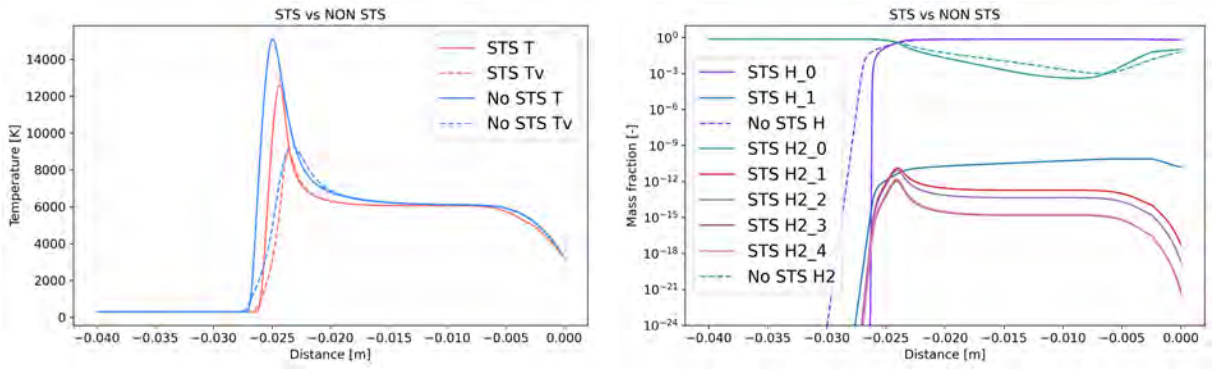

Figure 6: 2D flow over a cylinder results comparison between multi-temperature and pseudo-STS models. Temperature profiles *(left)* and mass fractions profiles *(right)* along the stagnation line. H_0, H_1 represent the ground state and the first electronic level for atomic hydrogen, respectively. $H2_0$, $H2_1$, $H2_2$, $H2_3$ and $H2_4$ represt the ground and excited states of molecular hydrogen.

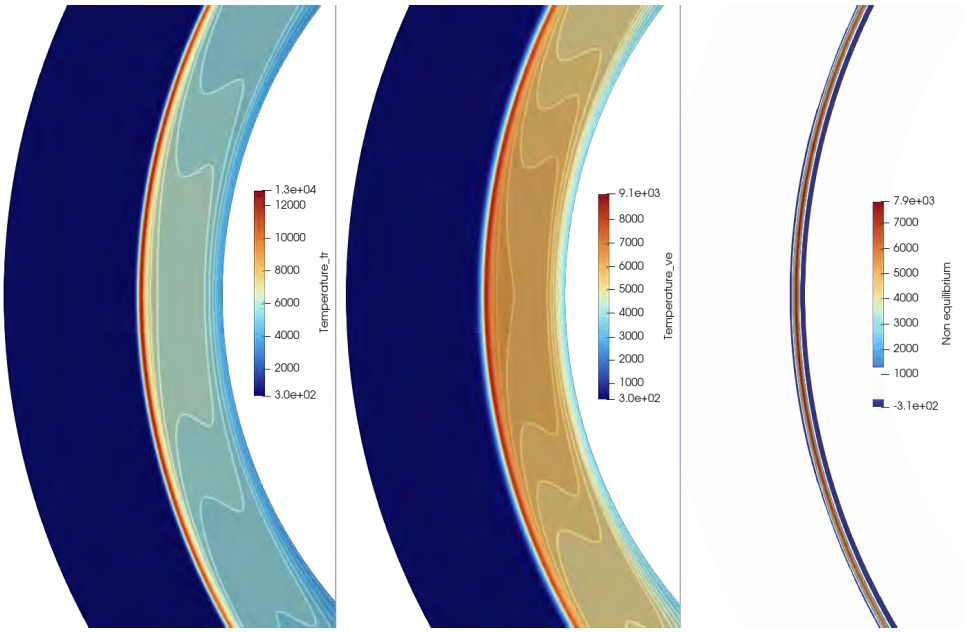

Figure 7: Thermal non-equilibrium contours. Translational temperature *(left)*, vibrational temperature *(middle)* and difference between the two *(right)*.

5. Conclusions

In this work, hypersonic non-equilibrium simulations of He/H_2 mixtures representative of Ice Giant atmospheric entry conditions were performed and compared against the DAMISO reference solver. The comparison focused on predicting the species distribution, and thermal non-equilibrium effects under high-enthalpy conditions. Overall, the results demonstrate a satisfactory agreement between SU2 and DAMISO, confirming the capability of the implemented framework to reproduce the dominant physical phenomena governing chemically reacting and thermally non-equilibrium flows. Nontheless, non-negligible discrepancies are observed in several flow quantities. These differences can be primarily attributed to the distinct thermodynamic modeling assumptions adopted by the two codes. In the present SU2 formulation, the electron temperature is assumed to be in equilibrium with the vibrational temperature, whereas DAMISO assumes it equals the translational temperature. Since ionization, recombination, and electron-impact processes are highly sensitive to the electron temperature, these different assumptions directly affect the predicted thermochemical state of the plasma and, consequently, the species concen-

trations and energy distributions throughout the flow field. The observed deviations should therefore not be interpreted solely as numerical differences between the solvers, but rather as a consequence of the different physical models employed to describe thermochemical non-equilibrium. The comparison highlights the importance of the electron-energy treatment in high-enthalpy hydrogen-helium plasmas and suggests that the choice of thermodynamic closure can significantly influence the predicted flow properties.

Acknowledgements

The authors wish to acknowledge the financial support of: ESA Cooperative Agreement No. 4000149949/25/NL/GLC: "Non-Equilibrium aerotherModynamics and ablatiOn: Coupling complex physics for destructive atmospheric re-entry". ESA CONTRACT No. 4000139351/22/NL/MG: "Development of a state-to-state CFD code for the characterization of the aerothermal environment of Ice Giants planets entry capsules".

The authors would like to thank the Polytechnic University of Bari for supporting this research activity. This work was developed within the framework of the Master's Degree program in Mechanical Engineering.

D. Ninni, F. Bonelli and G. Pascazio were partially supported by the Italian Ministry of Education, University and Research under the Program Department of Excellence Legge 232/2016 (Grant No. CUP - D93C23000100001).

6. Appendix A.

Table 5: Electron-impact excitation reactions.

No.	Type	Reac. 1	Reac. 2	Prod. 1	Prod. 2	Rate law
1.1	Electron-impact excit. H	H(0)	e^-	H(1)	e^-	`CNR_Bari_1`
1.2		H(0)	e^-	H(2)	e^-	
1.3		H(0)	e^-	H(3)	e^-	
1.4		H(1)	e^-	H(2)	e^-	
1.5		H(1)	e^-	H(3)	e^-	
1.6		H(2)	e^-	H(3)	e^-	
2.1	Electron-impact excit. H_2	$H_2(0)$	e^-	$H_2(1)$	e^-	CNR_Bari_4
2.2		$H_2(0)$	e^-	$H_2(2)$	e^-	
2.3		$H_2(0)$	e^-	$H_2(3)$	e^-	
2.4		$H_2(0)$	e^-	$H_2(4)$	e^-	

Table 6: Radiative reactions considered in this work.

No.	**Type**	**R1**	**R2**	**P1**	**P2**	**P3**	**Rate law**
1.1	Radiative recombination H^+	H^+	e^-	H(0)	$h\nu$		`CNR_Bari_1`
1.2		H^+	e^-	H(1)	$h\nu$		
1.3		H^+	e^-	H(2)	$h\nu$		
1.4		H^+	e^-	H(3)	$h\nu$		
2.1	Bound-bound emission H_2	$H_2(1)$		$H_2(0)$	$h\nu$		`constant`
2.2		$H_2(2)$		$H_2(0)$	$h\nu$		
2.3		$H_2(3)$		$H_2(0)$	$h\nu$		
2.4		$H_2(4)$		$H_2(0)$	$h\nu$		
3.1	Bound-bound emission H	H(3)		H(0)	$h\nu$		
3.2		H(3)		H(1)	$h\nu$		
3.3		H(3)		H(2)	$h\nu$		
3.4		H(2)		H(0)	$h\nu$		
3.5		H(2)		H(1)	$h\nu$		
3.6		H(1)		H(0)	$h\nu$		
4.1	Photo-dissociation H_2	$H_2(1)$		H(0)	H(0)	$h\nu$	
4.2		$H_2(2)$		H(0)	H(0)	$h\nu$	
4.3		$H_2(3)$		H(0)	H(0)	$h\nu$	
4.4		$H_2(4)$		H(0)	H(0)	$h\nu$	

Table 7: Chemical reaction mechanism considered in this work.

No.	Type	R1	R2	P1	P2	P3	Rate law
1.1	Heavy-impact diss. H_2/H_2	$H_2(0)$	$H_2(*)$	$H(0)$	$H(0)$	$H_2(*)$	arrhenius
1.2		$H_2(1)$	$H_2(*)$	$H(0)$	$H(0)$	$H_2(*)$	
1.3		$H_2(2)$	$H_2(*)$	$H(0)$	$H(0)$	$H_2(*)$	
1.4		$H_2(3)$	$H_2(*)$	$H(0)$	$H(0)$	$H_2(*)$	
1.5		$H_2(4)$	$H_2(*)$	$H(0)$	$H(0)$	$H_2(*)$	
2.1	Heavy-impact diss. H_2/H	$H_2(0)$	$H(*)$	$H(0)$	$H(0)$	$H(*)$	CNRBari_2
2.2		$H_2(0)$	$H(1)$	$H(0)$	$H(0)$	$H(0)$	constant
2.3		$H_2(1)$	$H(*)$	$H(0)$	$H(0)$	$H(*)$	arrhenius
2.4		$H_2(2)$	$H(*)$	$H(0)$	$H(0)$	$H(*)$	
2.5		$H_2(3)$	$H(*)$	$H(0)$	$H(0)$	$H(*)$	
2.6		$H_2(4)$	$H(*)$	$H(0)$	$H(0)$	$H(*)$	
3	Heavy-impact diss. H_2/He	$H_2(0)$	He	$H(0)$	$H(0)$	He	CNRBari_2
4.1	Electron-impact diss. H_2	$H_2(0)$	e^-	$H(0)$	$H(0)$	e^-	CNRBari_3
4.2		$H_2(0)$	e^-	$H(0)$	$H(1)$	e^-	
4.3		$H_2(0)$	e^-	$H(0)$	$H(2)$	e^-	
5	Electron-impact diss. H_2^+	H_2^+	e^-	$H(0)$	H^+	e^-	CNRBari_1
17	Heavy-impact elec. detach. H^-/H_2	H^-	$H_2(0)$	$H(0)$	e^-	$H_2(0)$	
19	Heavy-impact elec. detach. H^-/He	H^-	He	$H(0)$	e^-	He	arrhenius
20.1	Dissociative rec. H_2^+	H_2^+	e^-	$H(0)$	$H(1)$		CNRBari_1
20.2		H_2^+	e^-	$H(0)$	$H(2)$		
20.3		H_2^+	e^-	$H(0)$	$H(3)$		
21	Dissociative rec. H_3^+	H_3^+	e^-	$H_2(0)$	$H(0)$		
22	Dissociative rec. H_3^+	H_3^+	e^-	$H(0)$	$H(0)$	$H(0)$	
23	Dissociative attach. H_2	$H_2(0)$	e^-	H^-	$H(0)$		CNRBari_3
24	Dissociative attach. H_2^+	H_2^+	e^-	H^+	H^-		CNRBari_1
25	Dissociative attach. H_3^+	H_3^+	e^-	H_2^+	H^-		
26	Electron-impact ioniz. H_2	$H_2(0)$	e^-	H_2^+	e^-	e^-	CNRBari_3
27.1	Electron-impact ioniz. H	$H(0)$	e^-	H^+	e^-	e^-	CNRBari_1
27.2		$H(1)$	e^-	H^+	e^-	e^-	
27.3		$H(2)$	e^-	H^+	e^-	e^-	
27.4		$H(3)$	e^-	H^+	e^-	e^-	
29	Electron-impact electron detach. H^-	H^-	e^-	$H(0)$	e^-	e^-	
32	Heavy-impact rec. H_3^+/H_2	H_3^+	$H_2(0)$	H^+	$H_2(0)$	$H_2(0)$	arrhenius
33	Exchange H_2^+/H_2	H_2^+	$H_2(0)$	H_3^+	$H(0)$		constant
34	Charge exchange H_2/H	H_2^+	$H(0)$	$H_2(0)$	H^+		
35.1	Charge exchange H^-/H^+	H^-	H^+	$H(1)$	$H(0)$		arrhenius
35.2		H^-	H^+	$H(2)$	$H(0)$		
36	Charge exchange H_2^+/H^-	H_2^+	H^-	$H_2(0)$	$H(0)$		
37	Charge exchange H_3^+/H^-	H_3^+	H^-	$H_2(0)$	$H_2(0)$		

Table 8: New rate laws used in this work

CNR-Bari 1	**CNR-Bari 2**
$\ln K_f = \ln \sum_{i=0}^{3} \exp\left\{a_i - \frac{T_i}{T_\eta} + n_i \ln T_\eta\right\},$ a_i, T_i, and n_i are constant coefficients.	$a_i = \ln \sum_{j=0}^{3} \exp\left\{a_{ji}^0 - \frac{a_{ji}^1}{T_\eta} + a_{ji}^2 \ln T_\eta\right\},$ $T_i = T_i^0 + T_i^1 \frac{\exp\left\{\frac{\ln T_\eta - T_i^2}{T_i^3}\right\}}{\exp\left\{\frac{\ln T_\eta - T_i^2}{T_i^3}\right\} + \exp\left\{-\frac{\ln T_\eta - T_i^2}{T_i^3}\right\}},$ a_{ji}^k, T_i^k, and n_i are constant coefficients.
CNR-Bari 3	**CNR-Bari 4**
$\ln K_f = \ln \sum_{i=0}^{2} \exp\left\{a_i - \frac{T_i}{T_\eta} + n_i \ln T_\eta\right\},$ $a_i = \ln \sum_{j=0}^{1} \exp\left\{a_{ji}^0 - \frac{a_{ji}^1}{T_\eta} + a_{ji}^2 \ln T_\eta\right\},$ $T_i = T_i^0 + T_i^1 \frac{\exp\left\{\frac{\ln T_\eta - T_i^2}{T_i^3}\right\}}{\exp\left\{\frac{\ln T_\eta - T_i^2}{T_i^3}\right\} + \exp\left\{-\frac{\ln T_\eta - T_i^2}{T_i^3}\right\}}, \quad i = 1,2$ a_{ji}^k, T_i^k, and n_i^k are constants.	$\ln K_f = K_f^0 + \sum_{i=1}^{2} K_f^i,$ $K_f^i = a_i \frac{\exp\left\{\frac{\ln T_\eta - b_i}{c_i}\right\}}{\exp\left\{\frac{\ln T_\eta - b_i}{c_i}\right\} + \exp\left\{-\frac{\ln T_\eta - b_i}{c_i}\right\}}, \quad i = 1,2$ $\alpha = \alpha^0 + \alpha^1 \ln T_\eta, \quad \alpha = a_1, b_1, c_1,$ $\alpha = \alpha^0 + \alpha^1 \frac{\exp\left\{\frac{\ln T_\eta - \alpha^2}{\alpha^3}\right\}}{\exp\left\{\frac{\ln T_\eta - \alpha^2}{\alpha^3}\right\} + \exp\left\{-\frac{\ln T_\eta - \alpha^2}{\alpha^3}\right\}}, \quad \alpha = a_2, b_2, c_2.$ α^k are constant coefficients.

7. Appendix B.

Free electron-heavy translation (ET) energy exchange:

This term models the elastic energy exchange between free electrons and heavy particles through a Landau-Teller relaxation term:

$$\dot{\Omega}^{\mathrm{ET}} = n_e \nu^{\mathrm{ET}} \frac{T_{\mathrm{tr}} - T_{\mathrm{fe}}}{T_{\mathrm{fe}}} \tag{16}$$

where n_e is the electron number density and ν^{ET} is the transfer frequency:

$$\nu^{\mathrm{ET}} = \sum_{i \in \mathcal{H}} n_i \nu_i^{\mathrm{ET}}. \tag{17}$$

For $H_2 - e^-$, $H - e^-$ and $He - e^-$ interactions the fit from CNR-ISTP was used:

$$\ln \nu_i^{\mathrm{ET}}(T_{\mathrm{fe}}) = \sum_{j=0}^{1} \sigma\left(\ln T_{\mathrm{fe}}; a_{ji}, b_{ji}, c_{ji}\right) + d_i \tag{18}$$

whereas in the case of ions ($H^+ - e^-$, $H_3^+ - e^-$, $He^+ - e^-$):

$$\nu_i^{\mathrm{ET}} = \frac{2.6916624 \times 10^{-31}\, \mathcal{M}_{\mathrm{H}}}{\sqrt{T_e}\, \mathcal{M}_i} z_i^2. \tag{19}$$

The sigmoid function σ in 18 is expressed as:

$$\sigma(\eta; a, b, c) = a \, \frac{\exp\left\{\dfrac{\eta - b}{l}\right\}}{\exp\left\{\dfrac{\eta - b}{l}\right\} + \exp\left\{-\dfrac{\eta - b}{l}\right\}} \tag{20}$$

Vibration-heavy translation (VT) energy exchange:

The energy exchange between vibration and translation modes is of utmost importance in the relaxation process behind strong shock waves. The transfer term reads:

$$\dot{\Omega}_i^{\mathrm{VT}} = \rho_i \, \frac{e_i^{\mathrm{v}}(T_{\mathrm{tr}}) - e_i^{\mathrm{v}}(T_{\mathrm{v}})}{\tau_i^{\mathrm{VT}}} \tag{21}$$

$$\dot{\Omega}^{\mathrm{VT}} = \sum_{i \in \mathcal{V}} \dot{\Omega}_i^{\mathrm{VT}}, \tag{22}$$

here $\mathcal{V}$ is the group of vibrating species. The term τ_i^{VT} is the relaxation time and, for the $H_2 - H_2$, $H_2 - H$ and $H_2 - He$ collisions, is derived by the fit by CNR-ISTP:

$$\ln\left(p \, \tau_i^{\mathrm{VT}}(T_{\mathrm{v}}, T_{\mathrm{tr}})\right) = \sum_{j=0}^{3} \mathcal{K}_j \tag{23}$$

$$\mathcal{K}_j = \sigma\left(\ln T_{\mathrm{v}}; a_j, b_j, c_j\right), \qquad j = 1, 2, 3 \tag{24}$$

$$\alpha = \alpha^0 + \sum_{k=0}^{2} \sigma\left(\ln T; a_\alpha^k, b_\alpha^k, c_\alpha^k\right), \qquad \alpha = \mathcal{K}_0,\ a_j,\ b_j,\ c_j \tag{25}$$

where α^0, a_α^k, b_α^k and c_α^k are tabulated coefficients.

Electron-impact processes:

Electron-impact ionization (EI) and dissociation (ED) act as sinks to the vibration energy equation and are expressed in the following:

$$\dot{\Omega}^{\mathrm{EI}} = \sum_{r \in \mathcal{I}} \Delta\mathcal{H}_r \, \mathcal{R}_r, \tag{26}$$

$$\dot{\Omega}^{\mathrm{ED}} = \sum_{r \in \mathcal{D}} \Delta\mathcal{H}_r \, \mathcal{R}_r. \tag{27}$$

$\mathcal{I}$ and $\mathcal{D}$ are the ionization / recombination and the dissociation reaction sets, respectively.

Chemistry-vibration coupling:

The vibrational energy of the gas mixture is affected by the creation and destruction of molecules. The model approach used in this work is that of Candler [20] which assigns equal probability to a molecule dissociating from any vibrational state. The average change in the vibrational energy is equal to the average vibrational energy for the molecule regardless of energy distribution. For every molecular species:

$$\dot{\Omega}_i^{\mathrm{CV}} = e_i^{\mathrm{v}} \, \dot{\omega}_i \tag{28}$$

Bound-bound emission:

A heavy species in the j-th excited level emits radiative power (i.e. photon emission) spontaneously de-exciting to a lower energy level i. In this work, this is modeled considering an optically thin plasma

to all emission:

$$\dot{\Omega}^{\mathrm{BB}} = \sum_{k\in\mathcal{H}} \sum_{\substack{i,j\in\mathcal{E}_k \\ j>i}} n_k^j \, A_k^{ji} \left(e_k^j - e_k^i\right), \tag{29}$$

where the terms $\mathcal{A}_k^{ij}$ are the Einstein coefficients.

Free-free transitions: The free-free term models the transfer between the plasma and the environment due to Bremsstrahlung emission. Electrons are decelerated when deflected by a charged particle converting their kinetic energy into radiation:

$$\mathrm{X}_k + \mathrm{e}^- \rightarrow \mathrm{X}_k + \mathrm{e}^- + h\nu, \tag{30}$$

where X_k is any charged particle ($k \in C$) being C the set of charged particles. The transfer term can be expressed considering the electrons at equilibrium:

$$\dot{\Omega}^{\mathrm{FF}} = -\frac{16\pi^2}{3\sqrt{3}} \sqrt{\frac{8k_{\mathrm{B}}T_{\mathrm{fe}}}{\pi m_e}} \frac{\bar{g}_{\mathrm{ff}} e^6}{m_e h \left(4\pi\epsilon_0 c\right)^3} n_e \sum_{i\in C} z_i^2 n_i = -1.43\times10^{-40} \bar{g}_{\mathrm{ff}} \, n_e \sqrt{T_{\mathrm{fe}}} \sum_{i\in C} z_i^2 n_i. \tag{31}$$

The term $\bar{g}_{\mathrm{ff}}$ is the Gaunt factor and is of order unity.

References

[1] Chul Park. Nonequilibrium hypersonic aerothermodynamics. *Nonequilibrium hypersonic aerothermodynamics by Park*, page 29860, 1989.

[2] G Colonna, F Bonelli, and G Pascazio. Impact of fundamental molecular kinetics on macroscopic properties of high-enthalpy flows: The case of hypersonic atmospheric entry. *Physical Review Fluids*, 4(3):033404, 2019.

[3] F Bonelli, G Pascazio, and G Colonna. Effect of finite-rate catalysis on wall heat flux prediction in hypersonic flow. *Physical Review Fluids*, 6(3):033201, 2021.

[4] G Colonna, M Tuttafesta, M Capitelli, and D Giordano. Non-arrhenius no formation rate in one-dimensional nozzle airflow. *Journal of thermophysics and heat transfer*, 13(3):372–375, 1999.

[5] Mario Capitelli, Roberto Celiberto, Gianpiero Colonna, Fabrizio Esposito, Claudine Gorse, Khaled Hassouni, Annarita Laricchiuta, and Savino Longo. *Fundamental Aspects of Plasma Chemical Physics: Kinetics, in Springer Series on Atomic, Optical, and Plasma Physics*, volume 85. Springer Science & Business Media, 2015.

[6] M Capitelli, I Armenise, and Claudine Gorse. State-to-state approach in the kinetics of air components under re-entry conditions. *Journal of thermophysics and heat transfer*, 11(4):570–578, 1997.

[7] Davide Ninni, Francesco Bonelli, Gianpiero Colonna, Annarita Laricchiuta, and Giuseppe Pascazio. Assessment of hybrid macroscopic/state-to-state model for numerical simulation of ice giant orbit insertion. *International Journal of Heat and Mass Transfer*, 249:127188, 2025.

[8] Gianpiero Colonna, Louis Walpot, Davide Ninni, Francesco Bonelli, Giuseppe Pascazio, Lucia Daniela Pietanza, and Annarita Laricchiuta. Multi-temperature model from state-specific data for hydrogen/helium mixture in high-enthalpy flows. *International Journal of Heat and Mass Transfer*, 259:128376, 2026.

[9] Gianpiero Colonna, Lucia Daniela Pietanza, and Annarita Laricchiuta. Ionization kinetic model for hydrogen-helium atmospheres in hypersonic shock tubes. *International Journal of Heat and Mass Transfer*, 156:119916, 2020.

[10] Walter T Maier, Jacob T Needels, Catarina Garbacz, Fábio Morgado, Juan J Alonso, and Marco Fossati. Su2-nemo: An open-source framework for high-mach nonequilibrium multi-species flows. *Aerospace*, 8(7):193, 2021.

[11] James B. Scoggins, Vincent Leroy, Georgios Bellas-Chatzigeorgis, Bruno Dias, and Thierry E.

Magin. Mutation++: Multicomponent thermodynamic and transport properties for ionized gases in c++. *SoftwareX*, 12, 2020.

[12] Giuseppe Pascazio, Davide Ninni, Francesco Bonelli, and Gianpiero Colonna. Hypersonic flows with detailed state-to-state kinetics using a GPU cluster. In *Plasma Modeling (Second Edition): Methods and applications*. IOP Publishing, 2022.

[13] Willem H Hundsdorfer, Jan G Verwer, and WH Hundsdorfer. *Numerical solution of time-dependent advection-diffusion-reaction equations*, volume 33. Springer, 2003.

[14] Debby Lanser and Jan G Verwer. Analysis of operator splitting for advection–diffusion–reaction problems from air pollution modelling. *Journal of computational and applied mathematics*, 111(1-2):201–216, 1999.

[15] Gilbert Strang. On the construction and comparison of difference schemes. *SIAM journal on numerical analysis*, 5(3):506–517, 1968.

[16] James B Scoggins and Thierry E Magin. Development of mutation++: Multicomponent thermodynamic and transport properties for ionized plasmas written in c++. In *11th AIAA/ASME joint thermophysics and heat transfer conference*, page 2966, 2014.

[17] Joel H Ferziger and HG Kaper. *Mathematical Theory of Transport Processes in Gases.[By] JH Ferziger and HG Kaper*. North-Holland Publishing Company, 1972.

[18] Domenico Bruno, C Catalfamo, M Capitelli, G Colonna, O De Pascale, P Diomede, C Gorse, A Laricchiuta, Savino Longo, D Giordano, et al. Transport properties of high-temperature jupiter atmosphere components. *Physics of Plasmas*, 17(11), 2010.

[19] EA Mason, RJ Munn, and Francis J Smith. Transport coefficients of ionized gases. *The Physics of fluids*, 10(8):1827–1832, 1967.

[20] Graham V Candler and Robert W MacCormack. Computation of weakly ionized hypersonic flows in thermochemical nonequilibrium. *Journal of Thermophysics and heat transfer*, 5(3):266–273, 1991.